JOURNAL OF SPACECRAFT AND ROCKETS
Vol. 33, No. 5, September–October 1996

Space-Station Breadboard Beta Gimbal Assembly: Thermal-Vacuum Testing and Analyses

Shek-se P. Ip*
Rockwell International, Canoga Park, California 91309-7922

The objective of thermal-vacuum testing of the breadboard beta gimbal assembly is to demonstrate that the design can survive the hot–cold environment of the space-station mission and to check the fidelity of the thermal model for the beta gimbal assembly. The maximum deviation of the analyses from test data was less than 17°C. Only a few deviations were over 11°C, and most were within the recommended 14°C analysis margin. The predictions of the assembly's specific characteristics were confirmed by the test data. An exact match, however, is impossible because the testing boundary conditions are more complicated than on-orbit flight conditions. Also, there are uncertainties about the details of the thermal model. The black and Kapton® adiabatic coupons confirmed that the chamber wall was at −118°C instead of −157°C. The black coupons are recommended for absorbed-flux measurement because a blackbody is the easiest and most accurate of all coatings to analyze. Using Kapton and bare aluminum coupons is not recommended until a better thermal-radiation solver is available. The test results also indicated the two different heat-sink designs, back-to-back and side-to-side, for the coupon yield no significant difference because of the thermocouple design.

Introduction

THIS paper documents validation of the beta gimbal assembly (BGA) and bearing, motor, and roll ring module (BMRRM) thermal models, under both thermal balance and transient conditions. It uses breadboard BGA thermal-vacuum/thermal-balance-and-transient (TV/TB&T) test[1–4] results obtained in the Martin Marietta Aerospace Group (MMAG) Space Simulation Laboratory Waterton plant, near Denver, Colorado. With these compatible results, the requirement that the BGA thermal design survive the space-station mission and that survivability be verified with analyses and backed up by test data was satisfied. The analytical methods described in this paper were developed under the Space Station Freedom (SSF) program. In March 1994, SSF was reconfigured to become International Space Station (ISS). However, the same BGA design is used for both configurations and the analyses are equally valid. Therefore, the new ISS electrical configuration is used to demonstrate the importance of the BGA in controlling the operation of photovoltaic (PV) modules.

ISS Electrical Configuration

The ISS electrical configuration (Fig. 1) contains major PV components outboard of two alpha gimbals. The alpha gimbals control rotation around the longitudinal axis of the ISS. Two PV modules are located on each side of the ISS. Each module is made up of two array wings (two solar-array blankets per wing), two mast canisters, two BGAs, an integrated equipment assembly (IEA), and a radiator. The beta gimbals control rotation around the longitudinal axis of the PV arrays. The module provides primary power to the space station. The IEA is the assembly on the module that provides power conditioning and energy storage.

Each BGA (Fig. 2) consists of a BMRRM (Fig. 3), a platform, an electronics control unit (ECU), and a sequential shunt unit (SSU). The beta gimbals rotate PV array wings to keep the blankets in a suntracking orientation together with the alpha gimbals. Power generated in the PV blankets is routed through the platforms to the rest of the PV module. The platform subassembly interfaces with the mast canister, SSU, ECU, IEA, and solar-array wing harness. ECUs and orbit replaceable units monitor and control power to both the beta gimbals and PV array wings. ECUs also provide feedback control for the position of the motor in the beta gimbals. The SSUs match available PV-array power output to primary-distribution-bus load demand, and also regulate the primary-bus voltage level during the insolation portion of the orbit.

Test Configuration

The BGA was mounted to the thermal-vacuum test fixture through top-plate attachment points on the platform. The thermal-vacuum test fixture, which the platform rests on, was mounted to the stainless steel rails of the chamber. Two 1.27 × 1.27-m lamp cages were positioned 0.61 m away from the IEA side ($-X$ side) and the SSU side ($+X$ side) of the platform. The lamp cage located at the $-X$ side had eighteen 500-W quartz lamps arranged in a 6 × 3 grid pattern. The lamp cage located at the $+X$ side had 12 lamps arranged in a 4 × 3 grid pattern. Two pairs of radiometers faced each lamp cage. Each pair of radiometers consisted of one primary and one redundant. The radiometers were placed midheight of the housing simulator, and normal to the $+X$ and $-X$ planes. Multilayer insulation (MLI) blankets were placed on the SSU ($+X$), ECU ($+Y$), mast canister connector ($-Y$), and mast canister ($-Z$) sides of the platform. Without interaction from these electronic components, the performance of the BGA and BMRRM can be evaluated. The detailed test setup is shown in Fig. 4.

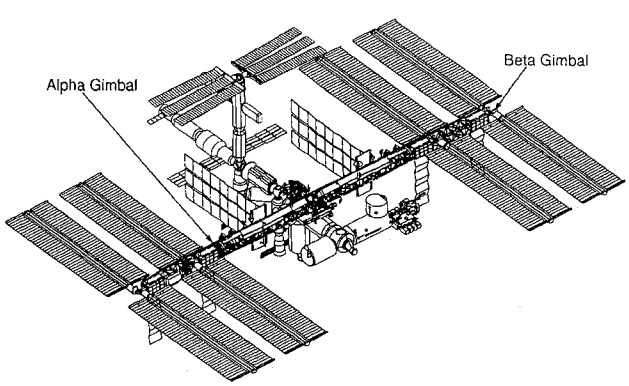

Fig. 1 ISS electrical configuration.

Received May 4, 1995; presented as Paper 95-2018 at the AIAA 30th Thermophysics Conference, San Diego, CA, June 9–12, 1995; revision received Jan. 15, 1996; accepted for publication Jan. 22, 1996.

*Heat Transfer Specialist, Rocketdyne Division, P.O. Box 7922, MS LA70.

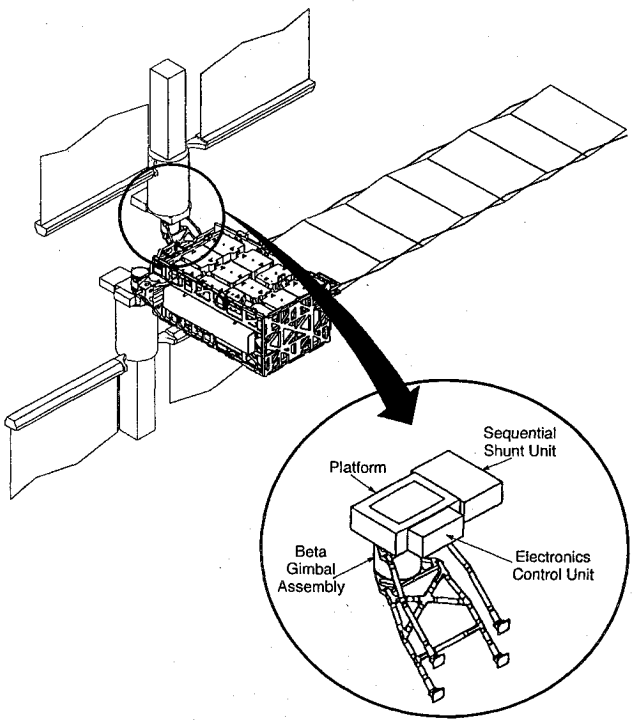

Fig. 2 IEA configuration with deployed solar arrays.

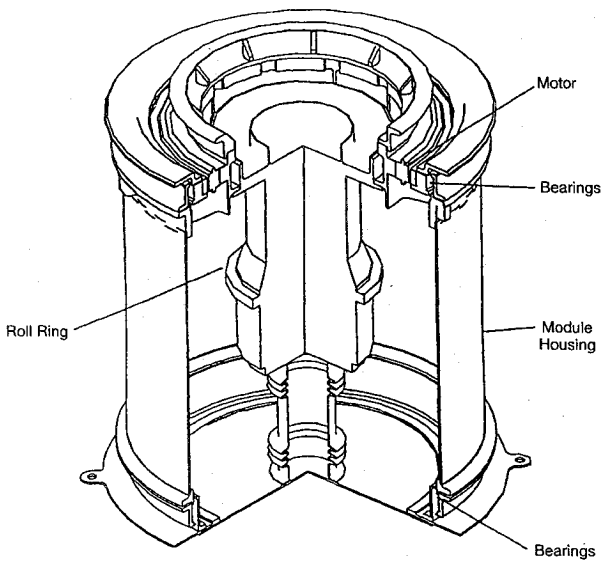

Fig. 3 BMRRM configuration.

Adiabatic Coupons

Adiabatic coupons[5] as an absorbed flux measurement device were fabricated from aluminum foil coated with three types of surface treatments: black paint, glued Kapton® film, and bare aluminum. Two kinds of heat-sink designs were tested: side-to-side and back-to-back. There were 12 black, 10 bare aluminum, and 10 Kapton coupons tested. These coupons were represented by 32 simple 0.38 × 0.38-m square surfaces. The optical properties (emissivity and solar absorptivity) of coupons with a similar design were measured by Lockheed Martin Vought System (Grand Prairie, Texas). Values are shown in Table 1.

Optical Coating Properties

Optical properties of the components in the thermal radiation analyzer system (TRASYS) models are summarized in Table 1.

TV/TB&T Test Environment

Absorbed solar, albedo, and planetary irradiation is simulated using heat lamps. To simulate the hottest and coldest environmental conditions induced on the BGA, the space-station dormant-stage configuration-1 (SC-1) and SC-17 local vertical, local horizontal flight modes were used. For cold and hot balance testing, orbital average heat fluxes (Table 2) (Ref. 2) were used. For the transient cycle test, the maximum solar and average Earth infrared (IR) radiation environmental constants were used. During the solar portion of the orbit, source power and secondary power were passed through the hardware (Table 3) (Ref. 2).

The SSU ($+X$) side of the platform was the only location available for adiabatic coupons without disturbing the TV/TB&T test. Therefore, neither the location nor the heat flux simulates any specific IEA orientation and environment conditions. The terms hot and cold, steady-state, and transient are defined with respect to the BGA. The heat flux the coupons experienced on the SSU side ranged from 0 to 568 W/m^2. Heat lamps were controlled to simulate all these heat fluxes and a (60 ± 0.5)-min solar and (30 ± 0.5)-min eclipse transient cycle.

Table 1 Properties of optical coatings

Component	Absorptivity	Emissivity
BGA housing simulator	0.95	0.92
BGA housing internal	0.35	0.85
Electrical cable	0.80	0.80
BFE cadmium connectors	0.40	0.11
Platform	0.40	0.80
Handrails	0.45	0.90
MLI	0.14	0.05
Interface fixture	0.92	0.84
Teflon® washer	0.25	0.85
Quartz lamps		
Tungsten filament	0.99	0.95
Quartz envelope	0.175	0.175
Reflector (lamp side)	0.18	0.05
Reflector (back side)	0.90	0.90
Adiabatic coupons		
Black paint	0.906	0.881
Aluminum	0.133	0.026
Kapton	0.337	0.845
Chamber	0.90	0.87

Table 2 Heat flux and current: hot and cold balance test[4]

Variable	Hot balance	Cold balance
$-X$-side flux, W/m^2	946 ± 32	221 ± 16
$+X$-side flux, W/m^2	155 ± 16	470 ± 16
Source current, A	178^{+0}_{-10}	±0
Secondary current, A	4.50 ± 0.5	0 ± 0
BGA motor current, A	0.55 ± 0.05	0 ± 0

Table 3 Heat flux and current: transient test[4]

Variable	Hot balance	Cold balance
Duration, min	60 ± 0.5	30 ± 0.5
$-X$-side flux, W/m^2	1419 ± 32	240 ± 16
$+X$-side flux, W/m^2	568 ± 16	0
Source current, A	212^{+0}_{-10}	2 ± 0.5
Secondary current, A	4.50 ± 0.5	$4.5^{+0.1}_{-0}$

Thermal Analysis Model

The pretest thermal model was built using the transparent-cage modeling technique. Because TRASYS is a diffuse-gray surface radiation solver, the intensity (heat flux) of the lamps must be measured. TRASYS[6] cannot accurately predict thermal radiation from quartz lamps, because it depends on the spectrum (wavelength), intensity, and interference. Thermal mapping of the test setup was performed[2] to ascertain pretest model boundary conditions. The BGA outer housing consisted of 88 measurement locations, and the platform had 196. The transparent-cage model assumed the blockage created by the lamp cages was 8% of the total area enclosed by the $+X$ lamp cage and 12% for the $-X$ lamp cage (Fig. 5). The model incorporated the BGA submodel, MMAG test chamber submodel, and test-interface–test-fixture submodel.

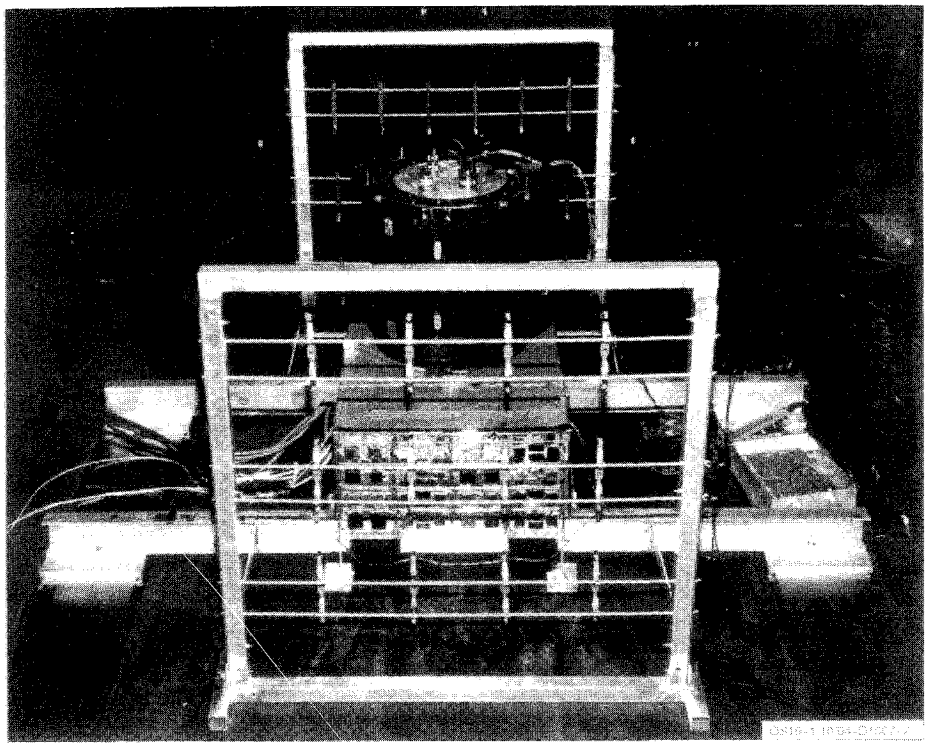

Fig. 4 BGA TV/TB&T test setup.

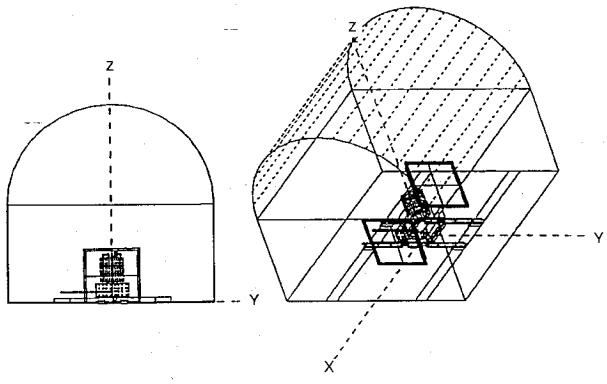

Fig. 5 TRASYS BGA transparent-cage model.

BGA and Test-Interface Submodel

The BGA[7] TRASYS and the systems improved numerical differencing analyzer (SINDA) and fluid integrator (FLUINT)[8] models included the latest design for the outer housing, BMRRM, platform, and Honeywell three-dimensional roll ring subassembly (RRS).[9,10] Minor modifications were made to this model to accommodate the TV/TB&T test-chamber condition. The beta-gimbal thermal-vacuum test fixture was modeled. Because the fixture was thermally insulated from the test hardware, its presence during the test did not have any significant influence on BGA temperatures.

MMAG Test-Chamber Submodel

The test-chamber TRASYS model was obtained from MMAG. The chamber is simply represented by a 4.9 × 5.5-m five-sided box as the floor and four sides of the shroud. The top is rendered by enclosed surfaces of a semicircular 5.5-m-long cylinder, 4.9 m in diameter (Fig. 5). Details of the portholes on the south side and blinds on the north side of the chamber were omitted by MMAG, because they were complicated and unknown before the start of test. The shroud was monitored by 54 thermocouples and controlled by five.

Test Data Evaluation

Data Management

Data reduction began once the lamps were powered on for the cold balance environment and ended after transient test was completed. The chamber pressure was reduced from ambient to 10^{-5} torr in 10 h. The cold steady-state environment was achieved in 29 h. The hot steady-state environment was achieved in 18 h, and seven cycles of hot and cold transient were completed in 10.5 h. Once every minute, 108 channels were automatically sampled and recorded. Each channel produced 3420 valid data points. Temperature-vs-time plots were compiled and checked for each channel. Data for each channel were separated into two time domains: cold–hot-balance test data and transient data. Red-line limits and vital data could be monitored independently through 30 parameters, which were recorded manually at half-hour intervals.

Radiometer Data

During cold cycles of the transient test, the radiometer facing $+X$ had readings as low as -66 W/m^2, which physically was incorrect. This phenomenon of the radiometer is explained in Ref. 11. The zero of the radiometer is not zero heat flux, but rather at a heat flux equivalent to the cooling-water temperature. The radiometer produces a negative signal for heat fluxes less than this value and a positive signal for fluxes greater than this value. This absolute heat flux is therefore dependent on measuring the cooling-water temperature at each radiometer. The zero output value of the radiometer depends on the cooling-water temperature; thus, the absolute calibration changes if the water temperature changes. The accuracy of the radiometers established by the manufacturer was calibrated against a known optical surface inside a theoretical black cavity. According to the radiometer manufacturer, no known analysis model can predict radiometer performance correctly.

Verification Methodology

The focus of the analysis is on verifying BGA thermal models. Before test, the original thermal model used transparent-cage methodology, a shroud temperature of -157°C, and values of the electrical power dissipation resistance values for a worst-case scenario (full power). The initial posttest analysis used the same model but incorporated actual test timelines. Pretest transient analysis predicted twice as much time for the hardware to reach cold steady state as the actual test time. This model gave satisfactory correlation of external BGA temperatures but did not match internal BMRRM temperatures, because the electrical power dissipation resistances of some components were obtained from maximum values from

the specifications and not from the actual measurements. Seven major iterations of model methodology and boundary conditions were generated during verification. Parameters for these iterations are the shroud temperature, electrical power dissipation resistance, radiometer heat-flux measurement, and quartz-lamp modeling.

Shroud Temperature

The initial analysis model was based on erroneous information[12] that the shroud temperature was a uniform −157°C because the shroud set-point temperature was maintained at −157°C throughout the test. Posttest investigation of the 54 shroud thermocouples revealed the average shroud temperature was −123°C. Additionally, the black (Fig. 6) and Kapton-coated adiabatic coupons implied that shroud temperature was −117°C.

Coupons were known to be facing the chamber wall (+X) throughout the test. During the cold cyclic transient, the coupons were exposed to no incident heat flux. Radiation exchange was the only mode of heat transfer between the coupons and the shroud; therefore, coupon data confirmed the analysis result that the shroud temperature was −118°C or warmer.

Quartz-Lamp Methodology

Quartz-lamp modeling does not depend on predetermined heat fluxes as a SINDA boundary condition. The quartz-lamp thermal model developed for the IEA TV/TB&T test[13] was used as a basis. Each quartz-lamp[14] model consists of a tungsten filament, a tubular quartz envelope, and a CERA-GOLD® semicircular stainless steel substrate reflector. The TRASYS thermal radiation solver will generate the view factor from the quartz-lamp model. In SINDA, either the lamp input power or the tungsten filament temperature is required. Using the filament temperature as boundary condition was found to work better than using the lamp input power as heat source in SINDA.

By matching adiabatic coupon temperatures with test data, and by varying the tungsten filament temperature as an independent variable, a simple correlation between lamp temperature and lamp input power was generated (Fig. 7). The correlation, which includes the incandescent effects, compared well with the literature,[14] even though the interpolation error could not be quantified. This method required only 1 h of VAX 9410 CPU time for a SINDA transient run.

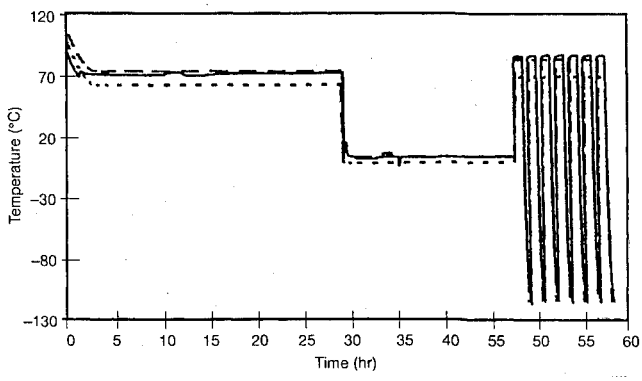

Fig. 6 Temperature profile of black adiabatic coupon (channel 233): ——, BK233; — —, trans. cages; and - - - -, quartz lamps.

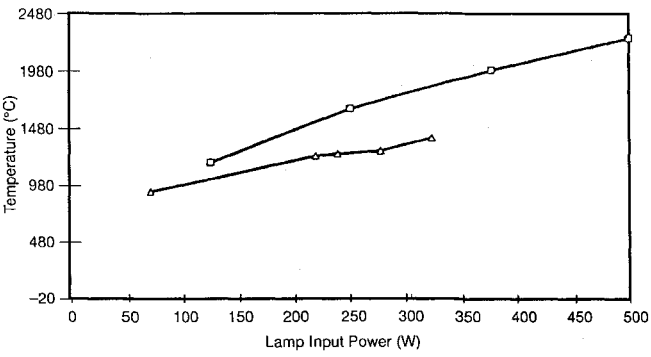

Fig. 7 Correlation of quartz-lamp temperature vs input power: □, lamp temperature and Δ, test configuration.

Analysis Results and Test Comparisons

Comparisons between test data and the two best-correlated model predictions are shown in Table 4. Only test data using thermocouples located on the outer housing, BMRRM, and RRS are shown. Graphical comparison of the locations to be discussed is shown in Figs. 8–10. Table 5 contains the description of these thermocouple locations. Table 4 is broken out into four time domains for comparisons: 1) steady-state cold, 2) steady-state hot, 3) last cycle of transient hot, and 4) last cycle of transient cold.

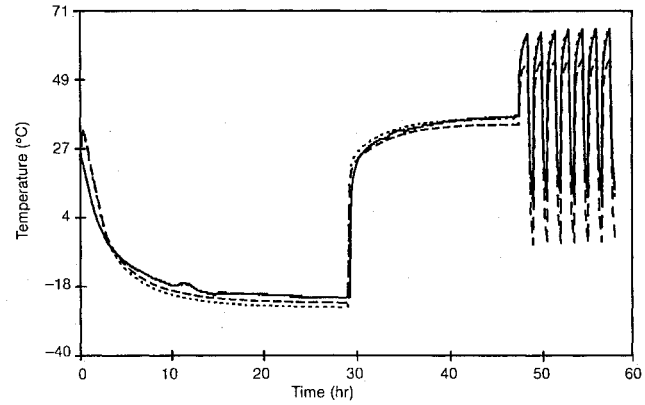

Fig. 8 BGA canistxer (−X) temperature comparison: ——, CH!49; — —, trans. cages; and - - - -, quartz lamps.

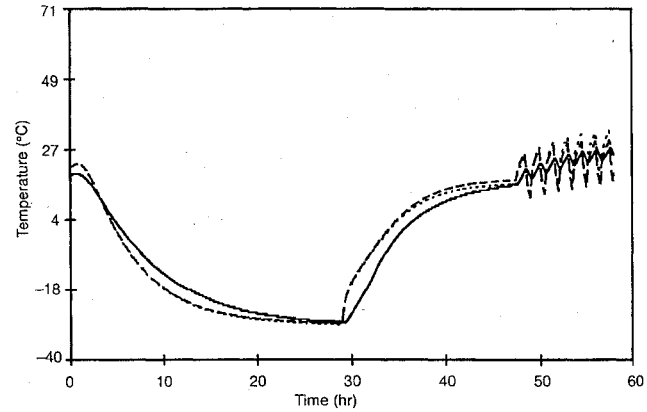

Fig. 9 Comparison of temperatures of source power at BFE connector: ——, CH!27; — —, trans. cages; and - - - -, quartz lamps.

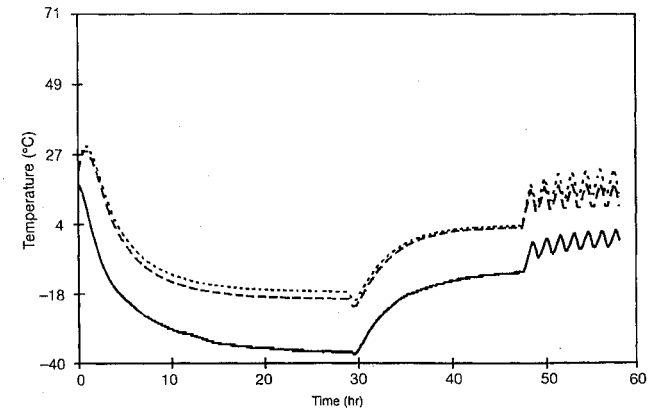

Fig. 10 Bearing support (+Y) temperature comparison: ——, CH117; — —, trans. cages; and - - - -, quartz lamps.

Table 4 BGA and RRS test and analyses temperature comparisons

	Steady-state cold			Steady-state hot			Transient hot[a]			Transient cold[a]		
		Model			Model			Model			Model	
Channel	Test, °C	Lamps, °C	Trans., °C	Test, °C	Lamps, °C	Trans., °C	Test, °C	Lamps, °C	Trans., °C	Test, °C	Lamps, °C	Trans., °C
					BGA							
101	−26	−16	−19	3	4	3	17	23	18	14	13	9
144	−24	−22	−24	2	19	18	17	38	31	12	23	16
145	−27	−27	−28	9	−17	−17	23	3	−2	18	−12	−16
106	−28	−36	−34	8	2	2	23	21	14	16	−2	−10
109	−30	−25	−24	0	9	13	12	23	23	12	20	20
110	−29	−26	−24	3	10	13	15	24	23	14	21	21
111	−24	−22	−24	11	19	17	26	37	29	21	23	16
112	−19	−17	−19	1	4	3	18	22	18	12	14	10
113	−26	−24	−23	8	6	7	22	20	17	19	18	16
114	−25	−25	−25	4	−1	−1	18	13	9	17	11	7
146	−24	−26	−24	6	9	12	18	23	21	17	21	20
115	−23	−25	−24	2	8	11	14	22	21	14	20	19
116	−38	−22	−24	−8	18	17	5	36	29	1	24	17
117	−37	−17	−19	−11	4	3	2	22	18	−1	14	11
149	−21	−24	−23	37	37	35	65	66	56	13	12	−3
147	−6	−3	−9	−7	−6	−8	26	26	19	−9	−13	−17
120	−28	−31	−30	−1	−6	−5	19	14	12	−2	−9	−14
123	−28	−31	−26	−2	−6	−4	18	14	12	−3	−10	−14
					RRS							
151	−28	−27	−27	12	7	9	22	19	17	22	19	17
152	−28	−28	−28	13	6	7	22	17	15	23	18	16
124	−28	−26	−24	8	8	11	19	21	20	19	20	19
153	−28	−28	−28	8	7	9	19	20	18	19	18	16
126	−28	−28	−28	15	6	8	26	19	17	24	17	14
127	−28	−29	−28	16	13	14	27	29	26	24	18	15
128	−28	−29	−28	15	16	17	26	33	29	24	18	15
129	−34	−27	−27	29	7	9	42	19	17	27	18	17
130	−31	−28	−28	7	6	8	18	19	17	17	17	14
131	−37	−29	−29	−4	−1	0	7	13	10	5	8	5
132	−37	−34	−33	−9	−13	−13	2	2	−2	1	−7	−11

[a]Last cycle.

Steady-State Cold

The thermal gradient across the outer housing and RRS can be verified only during the steady-state cold case. During that time, no current was passed through the RRS and motor, eliminating the confounding parameter of power dissipation. The temperature predictions for the RRS correlate better than the outer housing and BMRRM predictions for all models because change in external boundary temperatures had little effect on the RRS. Table 4 shows that magnitude differences were very small on the RRS: −7°C maximum deviation, averaging less than −2°C. The test data confirmed the analysis prediction that the RRS temperature is fairly uniform. The gradient across the outer housing (channel 147 minus 149) is 15°C, compared to the predicted 14°C using transparent-cage modeling, iteration 7. The −2°C difference is within the thermocouple tolerance of ±3°C; therefore, the steady-state cold results are within uncertainty limits. The prediction of the quartz-lamp temperature model, iteration 6, also compares well with the test data.

Steady-State Hot

Table 4 indicates moderate magnitude differences on RRS/BMRRM: the test data were +7°C maximum, +3°C average hotter than the predicted values. During the hot case, electrical power dissipation resistances take effect. Initial models were run with full-power dissipation values obtained from Honeywell's RRS model. The dissipation value was believed to be incorrect because the test temperatures in the RRS area were higher than actual temperatures even when using −157°C as the shroud temperature. Channels 127 and 128, located on the source power buyer-furnished equipment (BFE) connector and stator BMRRM interface, respectively, predict more than twice the test values. This finding triggered a parametric study of the power dissipation effect. When the dissipation value was adjusted to 23% of the original, the model temperature of the two channels dropped to the test value. However, channel 129,

Table 5 BGA and RRS components for test and analysis comparisons

Channel	Component
	BGA
101	Bottom BMRRM housing (−*X*)
144	Bottom BMRRM housing (+*X*)
145	Top BMRRM housing (−*X*)
106	Top BMRRM housing (+*X*)
109	Latch flange (−*Y*)
110	Latch flange (+*Y*)
111	Outboard attach flange (−*X*)
112	Outboard attach flange (+*X*)
113	Top retainer ring (+*X*)
114	Bottom retainer ring (+*X*)
146	Brushless dc motor (−*X*)
115	Brushless dc motor (+*X*)
116	Bearing support (−*X*)
117	Bearing support (+*X*)
147	BGA canister (+*X*)
120	BGA canister (+*Y*)
123	BGA canister (−*Y*)
	RRS
151	Secondary power module: stator
152	Secondary power module: rotor
124	Stator BMRRM interface (solar side)
153	Stator housing source power section (solar side)
126	Source power 1 cable
127	Source power at BFE connector
128	Stator BMRRM interface (antisolar side)
129	Stator housing source power section (antisolar side)
130	Stator housing source power section (solar side)
131	Secondary power cable
132	Secondary power at BFE connector

the source power section, measured 21°C hotter than predicted. This is a result of using a flat 23% power reduction factor. End-to-end resistance tests resulted in a flat 60% power reduction factor. Using a flat factor worked on only channels 127 and 128, but detailed component resistance and power values are needed to better correlate remaining primary power nodes of this model.

The RRS temperatures remained uniform during the steady-state hot condition. The RRS model predicts circumferential uniformity, which is true, except at the source power section of the stator housing (channel 129), which was hotter because of power dissipation. The predicted temperatures of the BMRRM bearings (channels 116 and 117) were higher than the test temperatures. The model had the motor current on, whereas in the test, it was off.

The quartz-lamp model, iteration 6, had the same outer-housing thermal gradient (44°C) as the test data. The iteration 7 model underpredicts the gradient by 9%. This result may be due to the lamps not being included in the local radiation exchange.

Transient

The transient hot cycle is the dominating cycle because the period (60 min) is longer than in the cold cycle (30 min). Also, the heat fluxes from the $-X$ side of the lamps are highest. The test data (Table 4) confirmed that there was no temperature variation in the RRS, and only slight variations in the BMRRM. However, a large thermal gradient (39°C) across the outer housing was observed. This trend is correctly predicted by the iteration 6 and 7 models. Once again, iteration 7 results underpredicted the gradient by 9%.

The driving force behind transient cold-cycle hardware temperatures was the residual heat effects of the hot cycle. The cold-cycle BMRRM housing and RRS temperatures were slightly lower than the hot cycle ones. The analysis models predicted this effect. During the iteration 6 parametric study, component temperatures of the hardware were found to be dependent on the lamp temperatures during the hot cycle. However, during the cold cycle, lamp effects can be ignored in comparison with the residual heat effects.

Performance of Iteration 6 and 7 Models

The iteration 6 (quartz lamp) prediction is closer to the test data than iteration 7, the heat-flux-adjusted transparent-cage model. Averaging the heat-flux input in iteration 7 provided better results than using local values without interpolations. The results are underpredicted except in the motor region, where they are overpredicted. With the modified power dissipation factor, RRS is slightly overpredicted except in the stator housing, secondary cables, and secondary power BFE connectors. Since one adjustment factor was used, some values of the power dissipation resistance are slightly off. Actual resistance measurements on key RRS hardware are required to upgrade the model. The iteration 6 and 7 models predicted the outer housing and RRS temperature values within the maximum and minimum analysis margin temperature, 14°C below hardware maximum values and 14°C above hardware minimum values.

Thermal Performance of the Adiabatic Coupons

During verification of the BGA thermal model, the performance of the adiabatic coupons was verified and they proved to be a valuable tool. Iterations 6 and 7 predicted the black coupons would have the best accuracy, followed by Kapton and bare aluminum. During hot and cold cyclic transient, the black coupons have the biggest temperature swings caused by heat-flux absorption, followed by the aluminum and the Kapton coupons (Fig. 11). These are explained by their absorptivity/emissivity ratios: the black coating has 1, aluminum 5, and Kapton only 0.4.

High-Heat-Flux Regimes

Since the quartz-lamp heat fluxes of the steady-state cold (470 W/m^2) and the hot cyclic transient (568 W/m^2) regimes are very similar, the test data indicate that thermal characteristics of the coupons behave nearly the same but with small variation in magnitude. Figure 12 shows the coupon coating, sensor design, and last cycle of hot-transient temperature. The thermal path of these coupons (Fig. 12) is transferred from the center of the platform to the sides ($\pm Y$) and from the top of the platform ($+Z$) toward the

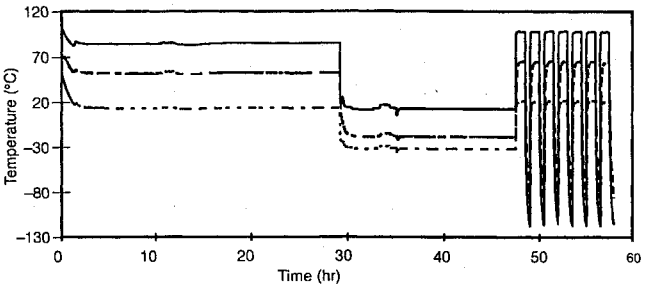

Fig. 11 Test comparison of black, Kapton, and bare aluminum coupons: ——, BK217; — —, KT222; and - - - -, AF225.

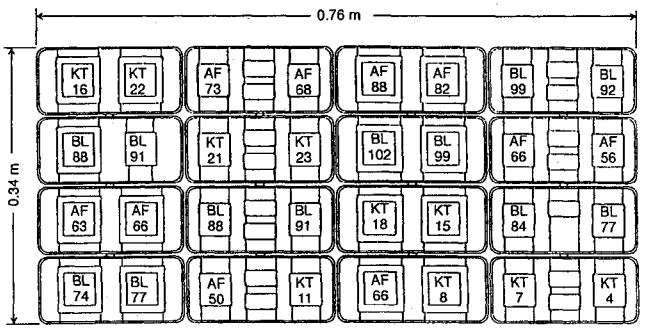

Fig. 12 Transient hot-test temperature (°C) of adiabatic coupons.

floor ($-Z$), because of the quartz-lamp arrangements and the different distances of heat sinks (shrouds) from the coupons. These phenomena are clear only when coupons with the same type of coating are compared. With this understanding of the difference between neighboring coupon temperatures, coupon sensor designs become obvious. Generally, in regimes with heat flux, black coupons are highest in temperature, followed by bare aluminum and Kapton coupons. The two thermal methodologies nicely predicted the test results on black adiabatic coupons, but the transparent-cage model slightly overpredicted the transient response, and the quartz-lamp model underpredicted the actual test data by 15%.

Zero-Heat-Flux Regime

The lamps were believed to simulate only the middle IR range, but the Kapton-coated coupon data indicate otherwise. Temperature of these coupons was approximately 30% of the black-painted coupons when the lamps were charged. This phenomenon indicates that the lamps were actually at the near-IR range, which is very close to the sun's intensity. If the wavelength of the lamps was at the middle IR range, then the Kapton-coated and black-painted coupons would have similar temperature readings because of similar emissivities. That was the case only during the cold-cyclic transient when the lamps ($+X$) were off.

Performance of the Thermal Models

From Ref. 15, the following results were observed. As expected, analysis models have the best performance for black coupons because of TRASYS specific diffuse-gray methodology. The Kapton optical coating characteristic was predicted correctly by the transparent model, but not by the quartz lamp model. The quartz-lamp model overpredicted Kapton coupon temperatures. For bare aluminum coupons, both analysis models overpredicted coupon temperatures. These are indications that TRASYS specular routines cannot analyze aluminum specularity correctly. Because no ISS structures are using bare aluminum, the importance is not a concern at this time.

Conclusions

The design requirement of the BGA thermal design—that it be able to survive the space-station mission and that the survivability be verified with analysis and backed up by test data—was satisfied. The BGA thermal-model predictions of the specific behavior of the outer housing, inner housing, RRS, and platform were

verified by test data. Absence of a circumferential thermal gradient across the RRS was confirmed by cold steady-state test data and analysis. The test also confirmed the analyses' predictions that the RRS would remain nearly constant during the 1-h hot and 0.5-h cold cyclic transient, because the RRS does not react to the external outer-housing condition after several cycles. Black coatings for absorbed-flux measurement are recommended for use in future TV/TB&T testing. Unless another thermal radiation solver such as the thermal synthesizer system is ready and verified with present BGA TV/TB&T test data, coatings other than black are not recommended. This thermal-vacuum test experience is likely to be very beneficial, especially to future BGA and integrated-equipment assembly qualification testings.

Acknowledgments

This work was supported by NASA Contract NAS3-25082. The author appreciated the courtesy and support of the Space Simulation Laboratory staffs at the MMAG Waterton plant, near Denver, Colorado, before and during the BGA thermal-vacuum test.

References

[1]Ip, S. P., "PV Breadboard BGA Thermal Vacuum/Thermal Balance Test Heat Transfer Analysis," Rocketdyne, IL 306-RP-IL94-033, Canoga Park, CA, May 1994.

[2]Vandel, S., O'Brien, D. L., and Ip, S. P., "PV Breadboard Beta Gimbal Assembly Thermal Vacuum/Thermal Balance Test and Heat Transfer Analyses Report," Rocketdyne, SSF ETD-PD4-A00489, Canoga Park, CA, June 1994.

[3]Vandel, S., "PV Breadboard Beta Gimbal Assembly Thermal Vacuum/Thermal Balance Test Procedure," Rocketdyne, SSF ETD-PD3-A00443, Canoga Park, CA, Feb. 1994.

[4]O'Brien, D. L., "PV Beta Gimbal Assembly Breadboard Development Thermal Vacuum Test Requirements," Rocketdyne, SSF ETD-PV1-A00309, Canoga Park, CA, Sept. 1993.

[5]Godinez, G., "IEA Thermal Vacuum/Balance Testing Heat Flux Sensor Development," Rocketdyne, IL 306-22-IL-93-085, Canoga Park, CA, Dec. 1993.

[6]Anon., "Thermal Radiation Analyzer System (TRASYS) User's Manual," NASA JSC-22964, April 1988.

[7]Kim, K., "Thermal Analysis of the Beta Gimbal Assembly, Space Station Freedom," Rocketdyne, IL 94-EPS-8F-002, Canoga Park, CA, Feb. 1994.

[8]Cullimore, B. A., Goble, R. G., Jensen, C. L., and Ring, S. G., "SINDA '85/FLUINT: Systems Improved Numerical Differencing Analyzer and Fluid Integrator User's Manual," Version 2.2, Martin Marietta Corp., MCR-86-594, Littleton, CO, Sept. 1988.

[9]Batista, J., "Engineering Drawings, Analysis, and Associated Lists for Beta Gimbal Roll Ring Subassembly (BGRRS), Analysis M-43 BGRRS Three Dimensional Transient SINDA Thermal Model Analysis," Rocketdyne, Subcontract Document No. 55E60123-065, Canoga Park, CA, Aug. 1993.

[10]Anderson, J., "Engineering Drawings and Associated Lists, Thermal Analysis for Beta Gimbal Roll Ring Subassembly (BGRRS)," Rocketdyne, Subcontract Document No. 55E60123-017, Canoga Park, CA, Dec. 1992.

[11]Durant, D. Q., and Fuld, C. J., "The Delta Star Thermal Vacuum Test: A Unique Approach to Space Thermal Simulation," *Proceedings of 18th Aerospace Testing Seminar*, Inst. of Environmental Science, Mt. Prospect, IL, 1991, pp. 203–214.

[12]Watson, R. N., and Bonn, J. W., "A New Thermal Vacuum Facility at the Martin Marietta Waterton Plant," *7th Space Simulation Conference Terrestrial Test for Space Success*, NASA Goddard Space Flight Center, Greenbelt, MD, 1992, pp. 165–182.

[13]Nguyen, L., "Assessment of the SPF IEA/PV Radiator Test Lamp Requirements," Rocketdyne, IL 304-BJ-IL93-034, Canoga Park, CA, Aug. 1993.

[14]Anon., "Infrared Heating Module Using Tungsten Quartz Lamps to Simulate Solar Heating in Environmental Chambers," General Catalog, Research Inc., Minneapolis, MN, Jan. 1996.

[15]Ip, S. P., "IEA Adiabatic Coupon Performance Evaluation," Rocketdyne, IL 306-RP-IL94-082, Canoga Park, CA, Aug. 1994.

I. E. Vas
Associate Editor